PCCP

PAPER

View Article Online
View Journal | View Issue

Cite this: *Phys. Chem. Chem. Phys.*, 2025, **27**, 18015

Plasmon-induced resonant energy transfer and flat band formation in Fe and Co doped Ni(II) hydroxide for efficient photocatalytic oxygen evolution

Benjamin W. Kaufold, [a] Parisa Nematollahi, *[b] Bernardo Barbiellini, [ce] Dirk Lamoen, [d] Arun Bansil, [e] Hana Cheng, [a] Sijia S. Dong *[aef] and Sanjeev Mukerjee *[a]

Received 16th March 2025,
Accepted 5th August 2025

DOI: 10.1039/d5cp01022e

rsc.li/pccp

Enhancing photocatalytic oxygen evolution is vital for renewable energy. In this work, we demonstrate how plasmon-induced resonant energy transfer (PIRET) from gold nanoparticles (AuNPs) to Fe- and Co-doped nickel hydroxide ($Ni(OH)_2$) can improve this process. PIRET involves the transfer of energy from excited AuNPs to nearby molecules, boosting their reactivity. We show that doping $Ni(OH)_2$ with Fe or Fe/Co results in a significant enhancement in photocatalytic activity, achieving a 72% increase in oxygen evolution reaction (OER) performance compared to pristine $Ni(OH)_2$ layered double hydroxide (LDH). In addition, a reduced optical band gap from 2.8 eV (pristine $Ni(OH)_2$ LDH) to 2.3 eV and the formation of flat bands was observed, enabling efficient energy transfer upon plasmonic nanoparticle integration and enhancing electronic properties. This supports that the PIRET mechanism is responsible for the increased OER performance. This study demonstrates the crucial role of PIRET in enhancing plasmonic energy transfer and the synergistic effects of doping and AuNP coupling. These findings highlight the broader potential of material engineering in advancing efficient and sustainable energy technologies.

1. Introduction

Nickel-based layered double hydroxides (LDHs) include nickel(II) hydroxide ($Ni(OH)_2$) and mixed metal salts with the composition $[Ma_{1-x}^{2+}Mb_x^{3+}(OH)_2]^{x+}\cdot[(A^{n-})_{x/n}\cdot yH_2O]^{x-}$ (ref. 1) (where Ma represents a divalent transition metal, Mb represents a trivalent one, and at least some proportion of Ma or Mb is nickel).[2] They are popular catalysts for reactions relevant to the production of clean fuel, such as the oxygen evolution reaction (OER) and hydrogen evolution reaction (HER). Both of these reactions ultimately aim to improve the efficiency and cleanliness of fuel consumption, which is crucial in addressing our current climate crisis. Specifically, these two reactions are the half-reactions involved in water splitting, utilized in solar fuel cells to directly generate energy stores from sunlight.[3]

Ni-based LDHs use earth-abundant transition metals and are more accessible than the expensive traditionally used catalysts, which often contain precious metals like platinum.[4,5] These LDHs are desirable not only for their accessibility but also for their performance, durability, and tenability. However, a few undesirable attributes, such as poor conductivity, still hinder the reactivity of these electrocatalysts towards water molecules. Therefore, diverse strategies can be used to control their properties like doping and synthetic conditions, leading to greater potential performance and the enhanced adsorption of oxygen-related intermediates.[6,7] It is known that doping $Ni(OH)_2$ with transition metal elements such as Fe and Co enhances their catalytic activity for OER compared to pristine $Ni(OH)_2$.[8–10] Doping results in shifting the Ni^{2+}/Ni^{3+} redox peak. For example, adding Fe increases the redox potential, while Co has the opposite effect.[11] These shifts have implications on both the onset and overall activity of OER in alkaline pH, as reported by Mukerjee *et al.*,[11] and Louie and Bell[12] in their studies on NiFe hydroxide thin films. Further insights were provided by Oliver-Tolentino and coworkers[13] in their comparisons of NiFeLDH and NiAlLDH. It has been reported that Fe is one of the two metals (alongside Mn) that maximally enhance the

[a] *Department of Chemistry and Chemical Biology, Northeastern University, Boston, MA 02115, USA. E-mail: s.dong@northeastern.edu, s.mukerjee@northeastern.edu*
[b] *Research Group MOSAIC, NANOlab Center of Excellence, Department of Chemistry, University of Antwerp, 2610 Antwerpen, Belgium. E-mail: parisa.nematollahi@uantwerpen.be*
[c] *Department of Physics, School of Engineering Science, LUT University, FI-53851 Lappeenranta, Finland*
[d] *Electron Microscopy for Materials Science (EMAT), NANOlab Center of Excellence, Department of Physics, University of Antwerp, 2020 Antwerpen, Belgium*
[e] *Department of Physics, Northeastern University, Boston, MA 02115, USA*
[f] *Department of Chemical Engineering, Northeastern University, Boston, MA 02115, USA*

electrocatalytic performance of $Ni(OH)_2$.[14] Incorporating Co, on the other hand, modulates the crystal structure of the hydroxides, enabling the formation of favorable interfaces between more conductive phases and more catalytically active ones.[15–18]

Plasmonic metal nanoparticles (PMNPs) such as Au, Ag, and Cu, have been explored to harness solar energy to improve catalytic properties. In heterogeneous catalysis, the distinction between surface plasmon resonance (SPR) and localized surface plasmon resonance (LSPR)[19,20] is relevant. The LSPR effect has been extensively reported in the context of electrocatalysis and water splitting, as observed in various configurations such as Au nanorods (AuNRs),[21] Au nanoparticles (AuNPs)[22] on MoS_2, and AuNP-decorated $Ni(OH)_2$ nanosheets ($Au{\cdot}Ni(OH)_2$).[23] This phenomenon has practical implications for the design of electrocatalysts using plasmonic effects, with considerations for charge injection. Interestingly, for heterogeneous catalysts where a semiconductor interfaces with PMNPs, two main mechanisms are possible, *i.e.*, (1) direct charge injection and (2) plasmon-induced resonant electron transfer (PIRET). In the PIRET mechanism, the coupled PMNPs work like antennae, harnessing light to generate charge carriers (electron–hole (e^-–h^+) pairs) *via* dipole–dipole coupling. This mechanism is proposed to explain the enhanced catalytic activity of the heterogeneous systems when the band gap of the donating atom in the catalyst is smaller than the excitation energy of the PMNPs.

Liu and coworkers[23] demonstrated in their work that it is possible to increase the catalytic performance of $Ni(OH)_2$ by decorating it with AuNPs and exposing it to laser light. Specifically, this increased and decreased the OER current and onset potential, respectively. To explain the influence of these conditions on OER, they invoke the LSPR phenomenon, where electrons on AuNPs oscillate in response to light with a proper frequency. They proposed that the laser light creates oscillating plasmons which are then conducted away. This creates a charge deficiency that cascades down from the AuNPs to the underlying $Ni(OH)_2$, thereby becoming more oxidative and effective at catalyzing OER. The presence of LSPR, a well-documented phenomenon under these conditions, suggests its contribution to the catalytic process.

Beyond replicating Liu's findings,[23] our study demonstrates that when $Ni(OH)_2$ is doped with Fe or with both Fe and Co, the OER current can be further enhanced through the LSPR mechanism and, moreover, that this process involves interactions between the electronic structure of Ni-based LDHs and AuNPs that have not been considered in ref. 23. By identifying features of the underlying catalyst that are responsible for producing more favorable coupling with the plasmons, we aim to gain insight into strategies for rational design of new catalytic systems based on the LSPR mechanism.

Due to the variability in the synthetic methods and structural phases, understanding the band structure of Ni-based LDHs is of major importance. In our experimental study, all samples of Ni-based LDHs were characterized, particularly those decorated with AuNPs showing light-driven OER enhancement. AuNPs were chosen as the representative PMNP owing to their favorable band gap and high corrosion resistance. This study aims to provide an explanation of the catalyst modification along with the resonant energy transfer mechanisms contributing to plasmonic-driven enhancement in OER. The work involves experimental and theoretical calculations to elucidate the nature of PIRET intervention in the OER mechanism.

2. Experimental procedures

The synthesized materials used in this work are as follows:[11] $Ni(OH)_2$, a layered double hydroxide with nickel as the sole transition metal, 3 : 1 NiFeLDH, where Ni^{2+} and Fe^{3+} are combined in 3 : 1 molar ratios during synthesis; 8 : 1 : 1 NiFeCoLDH, where Ni^{2+}, Fe^{3+} and Co^{2+} are combined in 8 : 1 : 1 molar ratios during synthesis; 9 : 1 NiFeLDH, where Ni^{2+} and Fe^{3+} are combined in 9 : 1 molar ratios during synthesis and AuNPs with an estimated average diameter of 5 nm.

Representative models for the materials $Ni(OH)_2$, 3 : 1 NiFeLDH and 8 : 1 : 1 NiFeCoLDH, which were used for computational purposes, are shown in the SI Fig. 1. To represent 8 : 1 : 1 NiFeCoLDH, it was deemed appropriate to use a model with 6 : 1 : 1 ratios of Ni : Fe : Co (hereafter referred to as 6 : 1 : 1 NiFeCoLDH) as modeling 8 : 1 : 1 NiFeCoLDH exactly required an impractically large model cell, shown in Fig. S2. We justify the use of the material with different metal ratios as an approximation for 8 : 1 : 1 NiFeCoLDH in this work.

In order to establish the proper magnetization of the LDHs, we use a set of "trial" magnetic configurations which are compared in Section 3.2.1 "geometric properties". The candidate magnetic configurations and the abbreviations used to refer to them are given in the SI Fig. S3.

The procedures for synthesizing and characterizing these materials as well as performing electronic structure calculations are given in the SI in the "Procedures for Materials Synthesis, Simulations, and Analysis" section. The synthesized AuNPs, the NiFeLDH decorated with AuNPs, the related absorption spectra, and the related tandem electron microscopy

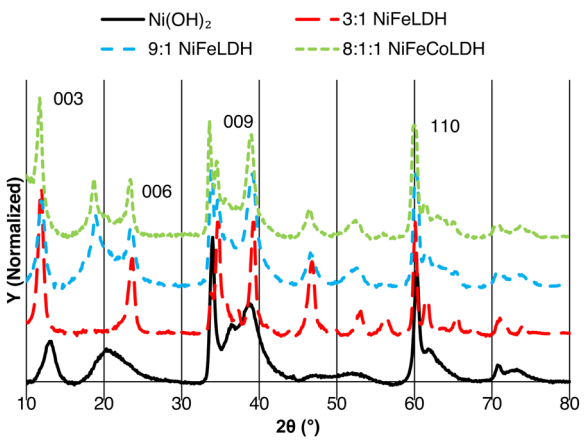

Fig. 1 X-ray diffraction spectra of the synthesized Ni-based LDHs, normalized to the same maximum intensity. Peaks corresponding to a rhombohedral cell are labeled with Miller indices.

(TEM) image are shown in Fig. S4 of the SI. Representative cyclic voltammagrams.

The absorption spectra confirm the formation of a chemical interface between the Ni-based LDH and AuNP. The amount of Au loading was determined using EDS data (Hitachi field emission SEM with EDAX). Au loading was 3.78%, 2.2% and 2.6% on $Ni(OH)_2$·Au, 9 : 1 NiFeLDH·Au and 8 : 1 : 1 NiFeCoLDH·Au samples respectively. The HR-TEM was measured using Thermofisher Titan Themis 300 S/TEM, 300 kV).

Surface areas of these samples have been published earlier (SI of ref. 11) and other similar publications.[24]

3. Results and discussions

3.1. Experimental results

3.1.1. X-ray diffraction. We conducted X-ray diffraction (XRD) measurements on four synthesized Ni-based LDHs, namely $Ni(OH)_2$, NiFeLDH (two different ratios), and 8 : 1 : 1 NiFeCoLDH. All of them exhibit peaks characteristic of a rhombohedral cell structure[25] as are labeled in Fig. 1. The occurrence of specific peaks exclusive to certain materials implies the presence of multiple phases that can only form in those materials with the appropriate proportion of metal ions. As an example, the sharp peak near $2\theta = 25^\circ$ labeled 006 is known to occur in other mixed nickel–iron layered double hydroxides.[25,26] In addition, this peak, as well as that near $2\theta = 12^\circ$, are directly tied to the interlayer spacing in the material.[27] The shifts in these peaks between the pure and doped materials suggest that adding dopants results in the formation of layered double hydroxide phases with different interlayer spacing. Especially interesting is that for those phases with low concentrations of dopants (9 : 1 NiFeLDH and 8 : 1 : 1 NiFeCoLDH), there appear to be two distinct peaks which could be assigned to the 006 Miller index, one with 2θ similar to that of $Ni(OH)_2$ and one similar to that in 3 : 1 NiFeLDH. A logical interpretation is that the 3 : 1 NiFeLDH has a layered double hydroxide crystal structure with a different interlayer spacing from $Ni(OH)_2$, and 9 : 1 NiFeLDH and 8 : 1 : 1 NiFeLDH contain some proportion of both this phase and the undoped $Ni(OH)_2$ phase. A significant peak broadening is observed in the spectra of all materials with $Ni(OH)_2$ exhibiting particularly pronounced broadening. This indicates the presence of extensive structural disorder across all phases.[28,29]

Interestingly, we found that adding AuNPs to the Ni-based LDHs does not change the observed XRD spectra significantly for 9 : 1 NiFeLDH and 8 : 1 : 1 NiFeCoLDH (see Fig. S5). This implies that the presence of AuNPs will not induce atomic-level changes in the semiconductor structures. Consequently, we extend the structural characteristics observed in the bare LDHs to their gold-decorated counterparts. Notably, due to the highly random morphology of AuNPs in our samples, the associated peaks in the XRD spectra will be small and broad, and blend with the background. In any case, it is more important that they do not influence the structure of the underlying semiconductors, so we may extrapolate any conclusions involving the structures of the undecorated materials to their decorated counterparts. We do so here in this work.

At this stage, we note some qualitative similarities between the spectra shown here and other layered double hydroxides in the literature. All of them share peaks with a NiMn layered double hydroxide with mixed α and β phases studied by Hall and coworkers[28] (besides a disagreement on the precise location of the 006 peak) as well as a NiFeCo hydroxide characterized by Attias and coworkers.[30] So, it is reasonable to claim that the underlying semiconductors, whether decorated with gold or not, are layered double hydroxides.

3.1.2. Structure fitting. As discussed before, the synthesized materials are likely multiphasic. Therefore, any single model cell used to represent them will be inherently inaccurate. We aim to construct model cells for each material, not to replicate them 1 : 1, but to approximate them well enough to gain insight into the electronic structure of the materials in computational studies. We use XRD analysis to justify that the model cells we have chosen for computational studies are good representations of the materials.

The calculated XRD spectra of the Dionigi-based models[31] of 3 : 1 NiFeLDH and α-$Ni(OH)_2$ fit the observed spectra of their synthesized counterparts using the Le Bail method[32] (see Fig. S6(a) and (b)). Using the Le Bail fitting technique, it was determined that our synthesized 3 : 1 NiFeLDH semiconductor can be modeled accurately using Dionigi's model, with an excellent match between the observed and calculated spectra. Similarly, our $Ni(OH)_2$ semiconductor closely resembles the α-$Ni(OH)_2$-like cell, constructed by substituting Ni atoms into Dionigi's model.[31]

The results of Le Bail fitting, the calculated XRD spectra of the Dionigi-based model of 6 : 1 : 1 NiFeCoLDH, and the observed spectra of the synthesized 8 : 1 : 1 NiFeCoLDH are demonstrated in Fig. S6(c). Despite the different compositions of the model and the real sample, we also show that there is a strong agreement between the XRD spectra obtained from the real material and those predicted by the model. In all cases, we have confirmed the use of the models as precise representations of the materials for predicting electronic structures *via* density functional theory (DFT) calculations. To determine the accuracy of the Le Bail fits spectra, we express the maximum difference between the fit and the corresponding experimental spectra (purple lines in Fig. S7 (a)–(c)) as a percentage of the maximum height of the experimental XRD spectra. The error in XRD fitting using this metric is 15% for 3 : 1 NiFeLDH, 32% for $Ni(OH)_2$, and 30% for 8 : 1 : 1 NiFeCoLDH.

We supplement our structure prediction of $Ni(OH)_2$ by performing phase quantification using the peak broadening of the 003 peak to determine the ratio of α and β phases in the sample. Using DIFFaX simulations by Rajamathi *et al.*,[29] it was found that the broadening of this peak (expressed as a ratio of peak width to height) correlates linearly with the proportion of phases in the sample, with the line of fit given in Fig. S7. We extend the extrapolated line of best fit to estimate that the $Ni(OH)_2$ sample contains the β phase in a proportion of only 26%, with the remainder being the α phase, resulting in a ratio

of α to β phases of 2.9 : 1. Given that the sample primarily exists in the α phase, it may be appropriate to employ an α-$Ni(OH)_2$-like cell to represent it. Moreover, it is consistent that a crystal cell primarily composed of α-$Ni(OH)_2$ should conform to the rhombohedral motif discussed earlier.[33] In the Electronic properties section, we will further discuss the use of the α phase rather than the β phase. The highly random, unpredictable nature of α-$Ni(OH)_2$ means we must consider the possibility that unusual features of our XRD spectra are caused by things other than, or in combination with, the formation of new crystal phases.

Given the good qualitative performance of the XRD spectrum fitting procedure for all materials, the phase quantitation of $Ni(OH)_2$ suggesting a primarily α-phase crystal, and the aforementioned literature support, we deem it appropriate to use the model cells we have chosen for representing the synthesized semiconductors in DFT calculations. The real materials may deviate from the models in terms of their lattice parameters, particularly the interlayer spacing. For instance, Dionigi and coworkers[31] demonstrated that the interlayer spacing of 3 : 1 NiFeLDH is different from that of 3 : 1 CoFeLDH and that the lattice parameters of both materials will change when they are oxidized. Furthermore, the model cells do not represent the suspected multiphasic nature of the materials, and we see in our $Ni(OH)_2$ phase quantification that there is about 26% β-$Ni(OH)_2$ in our sample. Where the model cells we constructed excel is in capturing the rhombohedral motif that all of our synthesized materials and similar materials in literature share.

3.1.3. Electrochemical measurements with plasmonic response. In the next step, all the synthesized LDHs are used as photocatalysts for catalyzing OER with and without the presence of AuNPs. Fig. 2(a) shows the OER response of undecorated LDHs. At the currents measured at a potential of 1.7 V *vs.* RHE, the activity of the catalyst for OER is very low. All the LDHs showed a minimal increase in current when exposed to laser light, except for 9 : 1 NiFeLDH which had a 10% increase. Coupling the catalysts with AuNPs, a significant OER enhancement is observed, more specifically on 9 : 1 NiFeLDH·Au with a 22% increase in current when exposed to laser light (see Fig. 2(b)). Thus, we can confirm that AuNPs work as antennae, capturing the light, and accelerating the transfer of electron–hole pairs which consequently leads to the OER enhancement.

Moreover, based on the cyclic voltammetry (CV) measurements, single doping with Fe and co-doping with Fe and Co (9 : 1 for NiFe LDH and 8 : 1 : 1 NiFeCoLDH) result in a reduction of the OER onset potential by 100–120 mV compared to both undoped $Ni(OH)_2$ and those doped solely with Co. At a voltage of 1.7 V, current measurements yielded a current density of approximately 10 mA cm^{-2} for doped catalyst samples and around 5 mA cm^{-2} for undoped ones. These values fall within the range of electrochemical data typically reported in the literature.[23,34] Our findings demonstrate that incorporating AuNPs into the modified $Ni(OH)_2$ catalyst, particularly 9 : 1 NiFeLDH, significantly enhances its photocatalytic properties

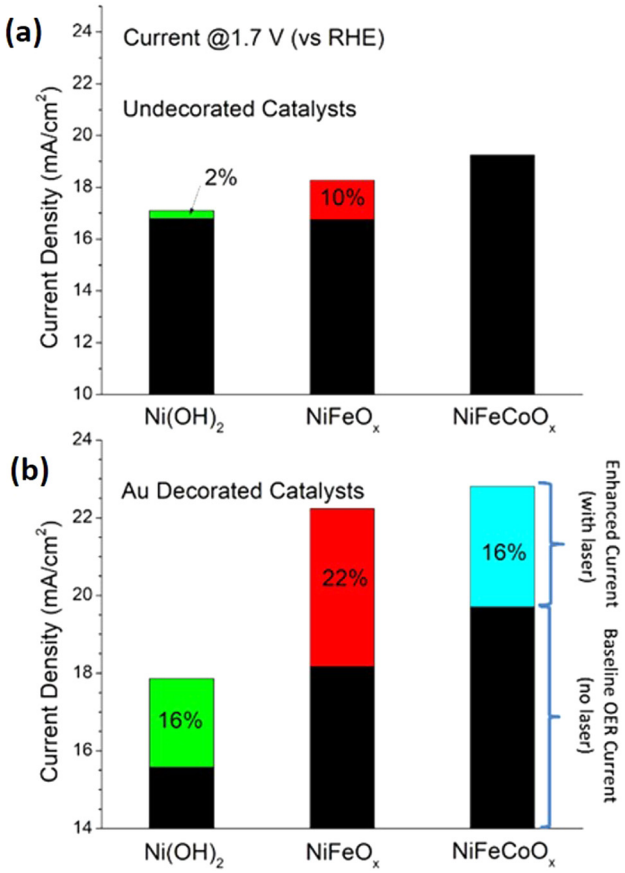

Fig. 2 Effect of Au coupling on the OER. (a) without AuNPs, (b) coupled with AuNPs.

for the OER. Our experimental evidence indicates that the electronic properties of the LDHs remain unaltered by the presence of AuNPs. Therefore, we can rely on the electronic properties of the LDHs without AuNPs. In the subsequent sections, we thoroughly explore the underlying factors contributing to the enhanced OER activity facilitated by AuNPs, an area of research that has received limited attention thus far. We conducted calculations to elucidate the underlying energy transfer mechanism responsible for the observed enhancement in the OER of the LDHs in the presence of AuNPs. The corresponding linear sweep voltammograms are in Section S8.

3.1.4. Diffuse reflectance. The diffuse reflectance spectra of the semiconductors highlight a significant distinction in the absorption profile between pristine $Ni(OH)_2$ and the doped LDH materials. Specifically, $Ni(OH)_2$ exhibits a steep absorption slope in the 300 nm to 200 nm wavelength range, whereas the slope is comparatively shallower in the doped materials (see Fig. 3).

The Kubelka–Munk (K–M) transformation was applied to the diffuse reflectance spectra to obtain the optical band gaps. The classical K–M model has been extensively employed[35] where Kubelka and Munk suggested that absorption and scattering are first-order phenomena.[36] Currently, K–M model is used to estimate the optical gap of the semiconductor materials to convert the diffuse reflectance into the absorption

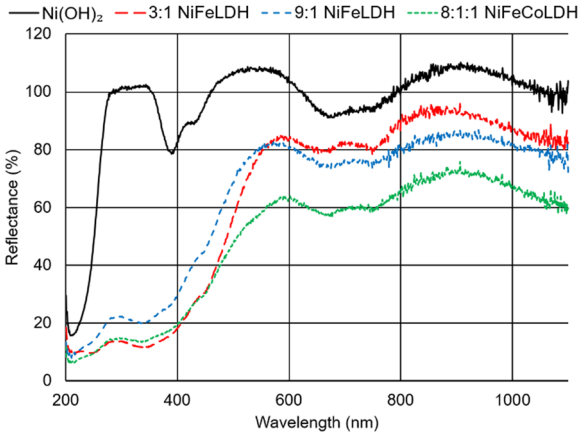

Fig. 3 Reflectance spectra of various synthesized semiconductors as a function of wavelength.

coefficient *via* the following equation:

$$\alpha \approx \frac{K}{S} = \frac{(1-R)^2}{2R} \equiv F(R) \quad (1)$$

where K and S are the absorption and scattering coefficients, respectively. We determine the optical gap of each catalyst from the $F(R)$ plot *versus* energy (E). Then, we fit the linear portion of the curve by a straight line (see Fig. S9). One can see that the calculated optical gap of the $Ni(OH)_2$ is slightly decreased upon its coupling with AuNPs using the Kubelka–Munk transformation from 5.2 to 4.9 eV. The corresponding details about the use of $F(R)$ are given in the SI.

In contrast to the pristine $Ni(OH)_2$, the optical gap of the NiFeLDHs and 8 : 1 : 1 NiFeCoLDH is significantly decreased from 5.2 eV in pristine $Ni(OH)_2$ to 2.2–2.3 eV in the doped materials. This can be due to the doping effect with Fe or Fe and Co (see Fig. S10 and Table 1). This aligns with our observations indicating that the OER enhancement in the presence of AuNP is more pronounced for the doped LDH materials compared to pristine $Ni(OH)_2$. Doping of the materials results in occupied states in the band gap that reduces it to an effective value of approximately 2.5 eV which is very close to the plasmon energy of the AuNP. This resonant situation of PIRET leads to an efficient transfer of energy between the AuNP and the doped material, without any charge transfer.

3.2. Computational results

DFT calculations were employed to investigate the geometry, electronic, and optical properties of LDH materials, offering valuable insights into their characteristics. First, a preliminary part of the computations *i.e.*, the calculation of the magnetization of the LDH catalysts and the optical gap has been done using CASTEP[37] code and the results are reported in the SI. Then, a detailed geometric optimization was performed in VASP[38] to confirm the trustworthiness of the model cells used. Finally, a comprehensive investigation of the magnetization, electronic, and optical properties of the LDH materials has been performed using the VASP code. The results are discussed in the following sections.

3.2.1. Geometric properties. We classified our calculations into two groups, *i.e.*, (i) the optimized configurations in which the unit cell and atomic positions of all structures are optimized and relaxed (Fig. 4), and (ii) the unoptimized configurations which are obtained from XRD spectrum fitting, and thus the position of atoms and the unit cell is fixed during the electronic and optical calculations. However, the geometrical refinement of these structures using PBE+U leads to similar lattice parameters compared to experiments with negligible atom displacement of <0.001 (see Fig. S11). It is therefore reasonable to assume that the unoptimized crystal cell geometries are close representations of the lowest-energy structures. As confirmed by Dionigi *et al.*,[31] these catalysts in their α-phase consist of Fe, Co, and Ni ions with different oxidation states within the layers of α-phase structures, where CO_3^{2-} and H_2O ions are intercalated between these layers[31] (see Fig. 4).

The magnetization of all the studied LDHs in their optimized and unoptimized state is investigated in detail. Different possible antiferromagnetic arrangements are considered for each structure. We found that optimizing the structures affects their anti-ferromagnetic properties, specifically on doped complexes. The results were similar to those obtained by CASTEP (given in Table S2) but the primary difference was that the optimized 3 : 1 NiFeLDH and unoptimized 6 : 1 : 1 NiFeCoLDH had a G-type and C-type ground state, respectively (see Tables S3 and S4). The observed difference is not significant, as the energies of the C-type and G-type states for this material are extremely similar in all cases. It is plausible that minor variations, such as changes in cutoff energy, k-point spacing, and whether geometry optimization has been performed, could potentially influence the order of these states.

For a better understanding of the reactivity of the LDH structures in connection with OER, binding energies for H

Table 1 Estimated optical gap in the LDH materials using the K–M transformation

Material	Optical gap (eV)
$Ni(OH)_2$	5.2
$Ni(OH)_2$·Au	4.9
3 : 1 NiFeLDH	2.2
9 : 1 NiFeLDH	2.3
8 : 1 : 1 NiFeCoLDH	2.2

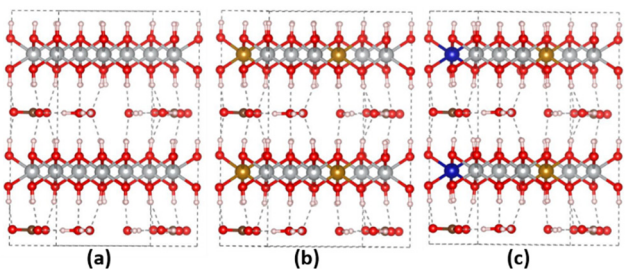

Fig. 4 The optimized configurations of α-$Ni(OH)_2$ (a), 3 : 1 NiFeLDH (b), and 6 : 1 : 1 NiFeCoLDH (c). Color code: red, O; gray, Ni; orange, Fe; blue, Co; white, H; and brown, C.

and OH were investigated using a slab of the LDH materials to which periodic boundary conditions were applied in the x and y directions. A vertical vacuum layer of 20 Å was added to minimize interactions between the slabs. All atomic positions were fully relaxed during the optimization process. H binding energy was calculated by introducing a H vacancy on the surface. H-vacancies considered in 3 : 1 NiFeLDH involved H removal from the O atom placed between the three Ni atoms (H_{NiNiNi}) or between the two Ni atoms and one Fe atom (H_{NiNiFe}) (see Fig. S12). H-vacancies considered in 6 : 1 : 1 NiFeCoLDH involved H removal from the O atom placed between the three Ni atoms (H_{NiNiNi}), or between the two Ni atoms and one Fe atom (H_{NiNiFe}), or between the two Ni atoms and one Co atom (H_{NiNiCo}) (Fig. S12). These configurations were also used for calculating the binding energy of the OH vacancy. Binding energies of H ($E_{b(H)}$) and OH ($E_{b(OH)}$) were calculated using:

$$E_{b(H/OH)} = E_{complex} - E_{defective\ complex} - E_{H/OH} \quad (2)$$

where $E_{complex}$, $E_{defective\ complex}$, and $E_{H/OH}$ are the calculated total energies of pure LDH, the defective H and OH configurations, and the energy of single H or OH atoms, respectively. The $E_{b(H)}$ and $E_{b(OH)}$ values so obtained for α-$Ni(OH)_2$ LDH, 3 : 1 NiFeLDH, and 6 : 1 : 1 NiFeCoLDH are −2.21, −0.47, −1.17 eV and −2.08, −3.21, −3.33 eV, respectively. Binding energies with smaller negative values (closer to 0) indicate a more favorable interaction between the gaseous species and the surface of the catalyst. Our results indicate that while the OH vacancy on the 3 : 1 NiFeLDH surface is less favorable for catalyzing the OER, the H-vacancy on the same surface makes the catalyst highly active for OER with a lower $E_{b(H)}$ adsorption energy of −0.47 eV.

According to the findings of Dionigi *et al.*,[31] there is a reversibility of the α-to-γ phase transformation by comparing the interlayer distances before and after increasing the potential. They believe that there is a contraction on both interlayer distances and in-plane bonds upon the transition of α-$Ni(OH)_2$ to its oxidized form γ-NiOOH along with all the other doped configurations. Although this contraction is for about 8%, they confirmed experimentally that only a fraction of the LDHs in their specific measurements undergo phase transitions under OER potentials. They explained that this might be due to the inaccessibility of some nanoplates in the catalyst's film with the electrolyte or the external electrical circuit. According to their investigations, the interlayer distances are calculated to be about 7.7 Å for both 3 : 1 NiFeLDH and 3 : 1 CoFeLDH. However, there has been no evidence to confirm the difference between the interlayer characteristics of the γ-NiOOH-type phase and other phases such as β-NiOOH-type phases.[39] Although these measurements were not the focus of our investigations, our calculations align well with those of Strasser's work.[31] We confirm a negligible contraction of the interlayer distance from 7.82 Å in the pure α-$Ni(OH)_2$ to 7.80 and 7.77 Å in doped structures of 3 : 1 NiFeLDH and 6 : 1 : 1 NiFeCoLDH, respectively. Consequently, this leads to a small contraction of local Ni–O, Fe–O, and Co–O distances for about 0.02 Å in doped structures which are not significant. Similarly, Kang *et al.*[40] found that in contrast to the traditional one-electron transfer in multilayer materials, in a monolayer $Ni(OH)_2$ nanosheet, a two-electron transfer occurs. They predicted that the first oxidation process $Ni^{2+} \rightarrow Ni^{3+}$ (from α-phase to the γ-phase) occurs easily while the second electron transfer $Ni^{3+} \rightarrow Ni^{4+}$ is strongly limited in multilayer materials. This can be due to the interlayer hydrogen bonds and also the domain H structure induced by the Jahn–Teller distortion of the Ni^{3+}-centered octahedral.

Moreover, we performed the Bader charge analysis[41] to calculate the charge density accumulation and depletion on the atoms, especially on the dopants. Our results indicate that upon doping, a great charge transfers from the dopants, Fe or Fe and Co, to the surrounding oxygen atoms. Table S5 lists the calculated Bader charges in each structure. One can see that in 3 : 1 NiFeLDH structure, there is a significant charge depletion and accumulation on Fe and O atoms, respectively, specifically on the atomic oxygen placed between two Ni atoms and one Fe atom, namely $O_{Ni-Fe-Ni}$. Introducing the second co-dopant, the Co atom, into the structure of 3 : 1 NiFeLDH, the same trend can be seen where the charges are mainly accumulated and depleted on Fe and $O_{Ni-Fe-Ni}$ atoms, respectively. While the Co atoms are subject to a greater charge depletion than the Ni Atoms in the 6 : 1 : 1 NiFeCoLDH structure, we estimate that the Fe atom is the main active site of the complexes. Thus, we confirm that single-atom doping into the pure structure of α-$Ni(OH)_2$ significantly enhances the charge transfer ability and consequently might have a considerable effect on the electronic and optical properties of the studied LDH materials.

3.2.2. Electronic properties. Our experimental investigations confirmed that doping $Ni(OH)_2$ (primarily α-phase) with Fe, or both Fe and Co, distinctly alters its electronic properties, irrespective of the inclusion of AuNPs. However, to have a better insight into the electronic properties of the LDH materials, detailed electronic calculations are performed. Tables S6 and S7 listed the calculated band gaps of both optimized and unoptimized LDH materials for configurations with both ferromagnetic and antiferromagnetic properties. Fig. 5 demonstrates the spin-polarized projected density of states (PDOS) split into contributions from individual O, Ni, Fe, and Co atoms. One can see in Fig. 5(a) that the energy difference between the valence band maximum and conduction band minimum for A-AFM α-$Ni(OH)_2$ structure is primarily composed of the Ni and O atomic orbitals, respectively, with the band gap of E_g = 3.67 eV (see Table S6). However, these results support our experimental observation that the band gap of undoped α-$Ni(OH)_2$ is larger than that of the doped materials. It is worth noting that while there are variations in band gaps between optimized and unoptimized structures, the overall trends remain consistent. The p orbitals of oxygen atoms and the d orbitals of Ni atoms are mainly below and above the Fermi level, respectively. This can also be seen in the corresponding band structure plot in Fig. 5(b). The peaks that cross the Fermi level of α-$Ni(OH)_2$ configuration might be related to the intercalated species. However, as we expected, pristine α-$Ni(OH)_2$ prohibits harvesting UV light (∼4 eV) due to its large band gap (∼5 eV).

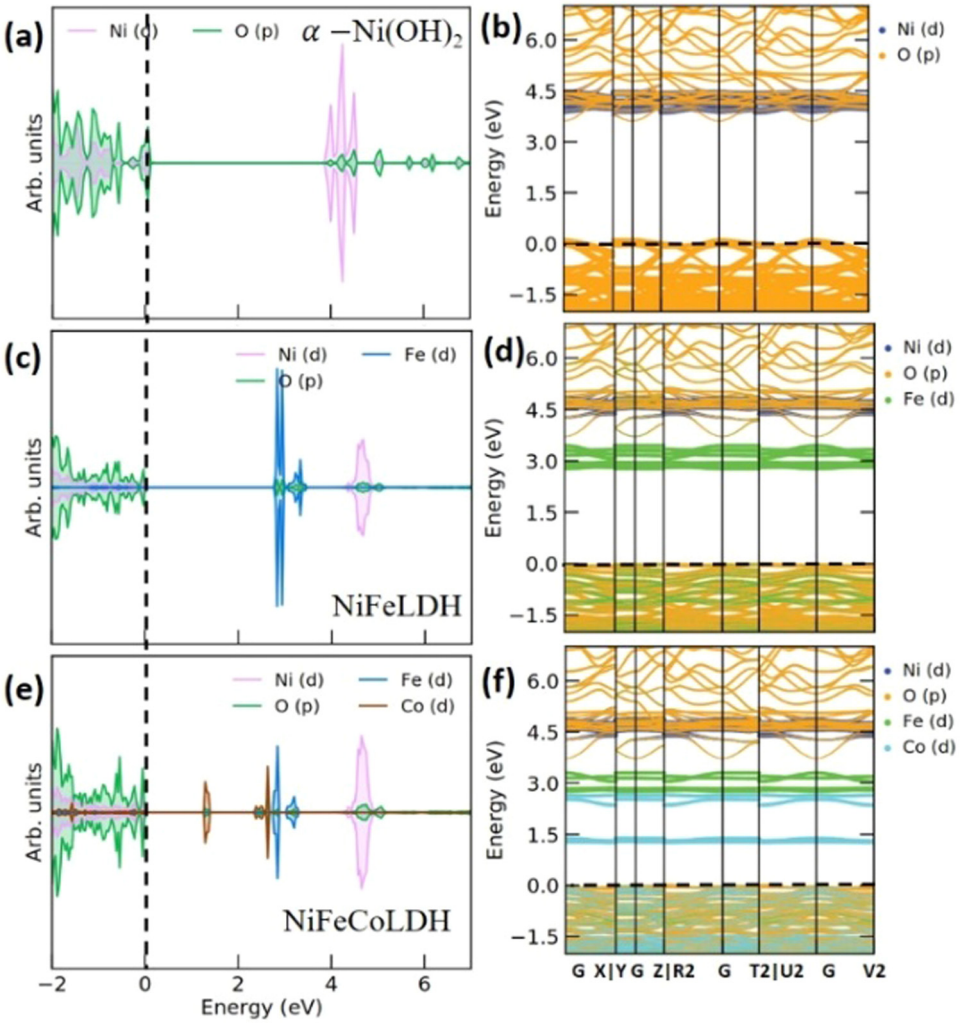

Fig. 5 PDOS and band structure of (a and b) α-$Ni(OH)_2$, (c and d) NiFeLDH, and (e and f) NiFeCoLDH.

Upon doping α-$Ni(OH)_2$ with Fe or with Fe and Co atoms, the band gap significantly reduces to 2.78 and 1.27 eV, respectively (Fig. 5(c) and (e)). This is due to the in-gap states originating from the hybridized d-orbitals of the doped transition–metal atoms with the p-orbitals of O in the doped structures in addition to the O hybridization with Ni d-orbitals, which can be seen in both the PDOS and the band structure plots. In 3 : 1 NiFeLDH, spin-up and spin-down peaks of Fe d-orbitals lie between the p-orbitals of O and the d-orbitals of Ni (Fig. 5(c) and (d)), while in 6 : 1 : 1 NiFeCoLDH the d-orbitals of Co appear between the d- and p- orbitals of Fe and O (Fig. 5(e) and (f)), respectively. This leads to a higher band gap reduction in 6 : 1 : 1 NiFeCoLDH. Note that the theoretical band gaps here are lower than the corresponding experimental values, which is to be expected due to the tendency of PBE+*U* to underestimate the band gaps in solids with tightly bound d electrons. Results for the unoptimized structures are similar (Table S7 and Fig. S13). While Fe is the main contributor to band engineering and photocatalytic activation in 3 : 1 NiFeLDH, the introduction of Co in 6 : 1 : 1 NiFeCoLDH provides distinct complementary effects. Our PDOS analysis shows that Co d-states appear between the Fe and Ni states, contributing to further band gap reduction and a more continuous density of states near the Fermi level. Moreover, Bader charge analysis suggests significant charge depletion on Co atoms, which enhances the local electric field around oxygen active sites. Although the reduction in interlayer spacing upon Co doping is minimal (from 7.82 Å in α-$Ni(OH)_2$ to 7.77 Å in 6 : 1 : 1 NiFeCoLDH), it may still influence the stability and ionic conductivity of the catalyst under electrochemical operation. Therefore, we propose that Co doping, while secondary in magnitude to Fe, enhances the performance of the LDH system by refining the band structure and contributing to improved electrochemical resilience. The PDOS analysis for unoptimized structures is given in the SI Fig. S14–S16 and largely confirms the above.

3.2.3. Optical properties

3.2.3.1. Optical absorption. To gain deeper insights into the photocatalytic properties of both pure and doped LDH structures, we analyze various representative plots to visualize their optical response. The optical properties are calculated from the

frequency-dependent complex dielectric function $\varepsilon(\omega) = \varepsilon_1(\omega) + \varepsilon_2(\omega)$ using the method of Gajdoš *et al.*,[42] where the $\varepsilon_1(\omega)$ and $\varepsilon_2(\omega)$ are the real and imaginary parts of the dielectric function, and ω is the photon frequency. Subsequently, the other optical properties *i.e.*, refractive index $n(\omega)$, loss function $L(\omega)$, reflectivity $R(\omega)$, and absorption coefficient $\alpha(\omega)$ can be computed from ε_1 and ε_2 (both are plotted and shown in Fig. S17 and an explicit expression of the optical quantities in terms of ε_1 and ε_2 is given in the SI). The calculated refractive index is shown in Fig. S18.

The photoconversion efficiency is of great importance for a photocatalyst. The calculated optical absorption plots of the pure α-$Ni(OH)_2$ and the tailored structures are given in Fig. 6(a). One can see that in the absence of AuNPs, all the materials absorb light mainly in the UV range. As was expected, α-$Ni(OH)_2$ has only marginal absorption in the visible light range. Although doping α-$Ni(OH)_2$ with Fe or both Fe and Co atoms has a great effect on their electronic properties, it has a negligible effect on their optical properties due to their marginal absorption in the visible range.

3.2.3.2. Optical gap (Kubelka–Munk transformation). Previously, we calculated the electronic properties of the catalysts and estimated the band gap of the materials. However, finding the optical gap of a semiconductor is also important for the determination of the wavelengths that activate the photocatalyst. Hence, we utilized the K–M transformation on our simulated absorption spectra, similar to our approach with experimental diffuse reflectance spectra, where absorption is directly used instead of being derived from reflectance.

The resulting absorption spectrum for α-$Ni(OH)_2$ is given in Fig. 6(b). The optical gap values obtained from the linear fits $F(R)^2$ and $F(R)^{1/2}$ *versus* E are in close agreement with our experimental finding that α-$Ni(OH)_2$ has a larger energy scale (>4 eV). This confirms that α-$Ni(OH)_2$ can hardly generates electron–hole pairs and resonate upon light illumination and therefore is inactive for OER. In doped catalysts, the energy scale reduces significantly to values of ≤ 2.5 eV, a minimum optical gap of a semiconductor that is being used for photocatalytic OER. This consequently enhances the electron current because of light illumination and the OER (Fig. 6(c) and (d)). We confirm that Fe or Fe and Co doping into the α-$Ni(OH)_2$ structure has a profound effect on the electrical and optical properties by reducing the fundamental and optical band gap that slightly facilitates the photocatalytic OER.

Although we experimentally confirmed the enhanced OER performance of Au-coupled LDH materials, we found that the electronic properties of the LDH materials remain unchanged when coupled with AuNPs. However, the presence of coupled AuNPs notably accelerates light absorption and energy transfer to the LDH materials, resulting in a significant enhancement of the OER process. The OER enhancement on similar structures

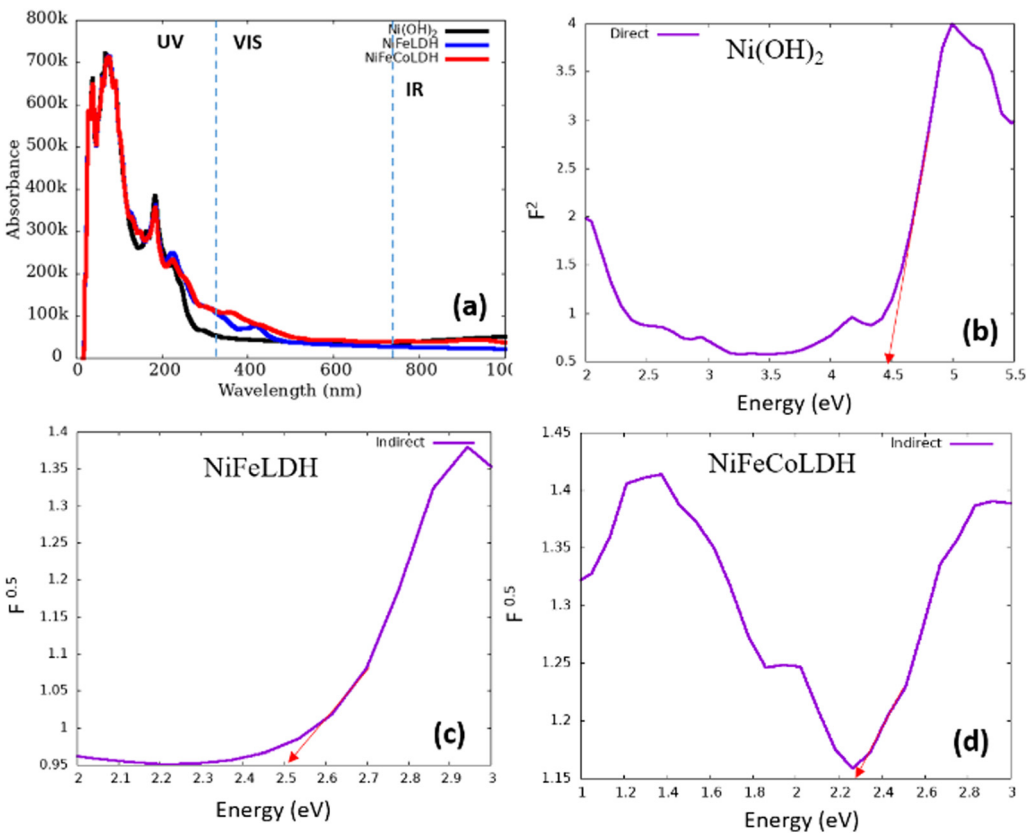

Fig. 6 (a) Simulated optical absorption spectra of LDH materials along with the corresponding theoretical K–M transformations for (b) $Ni(OH)_2$, (c) 3 : 1 NiFeLDH and (d) 8 : 1 : 1 NiFeCoLDH (using 6 : 1 : 1 NiFeCoLDH model).

has been previously investigated and reported.[43,44] Simulating these materials and elucidating the details of OER mechanisms are beyond the scope of this paper. Instead, our primary focus lies in the understanding of the origin of the energy transfer mechanism.

3.2.4. Role of plasmons in OER. The photocatalytic performance of semiconductors is highly dependent on their band energies.[45] It is known that the potentials of the photochemical OER (1.23 V) should straddle the conduction band and the valence band levels. Thus, the minimum band gap of a semiconductor that is being used for photocatalytic OER should be in the range of 1.9 to 2.3 eV considering the required overpotentials associated with thermodynamic losses.[46] Therefore, single semiconducting photocatalysts are not highly efficient for solar conversion. Additionally, using AuNPs coupled with a semiconducting photocatalyst forms an Au@semiconductor heterojunction that can significantly increase light absorption and has great potential in the catalyst's photosensitization.[19,20,47]

As we discussed in previous sections, the narrow band gap observed in the NiFeLDHs and 8 : 1 : 1 NiFeCoLDH renders them more suitable for application in photocatalytic OER compared to the pristine α-$Ni(OH)_2$ with a wider band gap. Our experimental and theoretical findings confirm that using AuNPs as plasmonic nanostructures on top of the LDH catalysts enhances the current density and consequently, increases their photocatalytic activity for OER (see Fig. 2).

Since we observe a plasmonic enhancement in undoped gold-decorated $Ni(OH)_2$, although it is less than that seen in doped materials, we acknowledge that multiple mechanisms, including the one we have proposed, are likely at play. To clarify the nature of the plasmon-induced enhancement, we considered both hot electron injection (HEI) and PIRET. According to our theoretical investigations, the conduction band minimum (CBM) of the doped LDH lies above the Fermi level of the plasmonic metal which makes the HEI energetically unfavorable. Furthermore, XPS and UPS data indicate negligible band bending or Schottky barrier formation at the metal–semiconductor interface, making HEI even more unfavorable. In contrast, the spectral overlap between the plasmon resonance and the LDH absorption edge, together with the unchanged absorption onset and the enhanced band-edge PL intensity, enhanced the possibility of a dominant PIRET mechanism. These results are consistent with previous reports[48–53] and indicate that energy transfer *via* (a non-radiative) dipole–dipole coupling controls the observed photocatalytic enhancement. The original mechanism proposed by Liu *et al.*,[23] is still valid for explaining the plasmonic enhancement seen for $Ni(OH)_2$. Additionally, Dionigi and coworkers[31] detail additional structural changes in the materials throughout oxidation that may change the mechanism as well. In doped materials, we propose that PIRET occurs simultaneously with other mechanisms, and the effects of plasmonic enhancement are additive.

3.2.5. The plasmonic energy transfer mechanism. PMNPs are well known to enhance solar energy conversion in semiconductors through three different mechanisms: light trapping, hot electron transfer, and PIRET. When the bandgap of the semiconductor is less than 2.5 eV and the plasmonic resonance of the metal falls within the visible or near-infrared (NIR) range, these plasmonic energy transfer mechanisms yield maximum solar energy conversion efficiency and enhanced catalytic activity.[19]

The plasmon's near field can non-radiatively excite charge carriers in the semiconductor *via* the PIRET mechanism. Coupling with PMNs doubles the photovoltaic and photoelectrochemical efficiency of the semiconductor.[48,49] Upon light absorption, the excitation of a plasmon in AuNP generates a dipole, which then drives the transfer of energy from the AuNP to the photocatalyst through the production and amplification of charge carriers *via* dipole–dipole interactions,[50,51] and results in an enhanced OER.

Our experimental observations and theoretical modeling confirm that $Ni(OH)_2$·Au carries smaller solar activity for OER than NiFeLDH·Au and NiFeCoLDH·Au, where the highest photocatalytic activity (22% of current density) is provided by NiFeLDH·Au. Fig. 5 and 7 show that the in-gap states introduced by the Fe dopants promote the PIRET mechanism and facilitate energy transfer from AuNPs to both the conduction and valence bands of the NiFeLDHs, which align well with the incident laser energy.[52,53] In contrast, the band gaps in α-$Ni(OH)_2$ and 8 : 1 : 1 NiFeCoLDH are not well aligned, which hinders the formation of high current densities. Fig. 7 indicates that an electron is transferred from an occupied oxygen band to

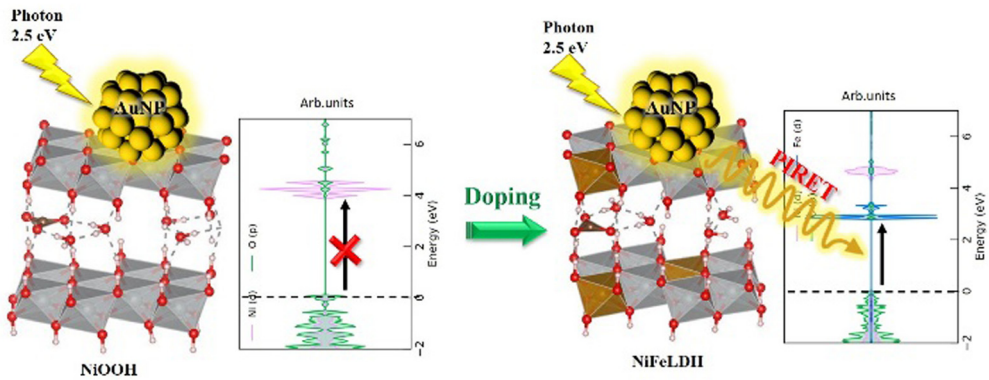

Fig. 7 A schematic illustration of the PIRET mechanism.

an empty Fe band in PIRET, but since oxygen is hybridized with Ni, the effective reaction is triggered by PIRET is: $Ni^{2+} + Fe^{3+} \rightarrow Ni^{3+} + Fe^{2+}$ the highly oxidized Fe^{3+} (ref. 54 and 55) state of iron makes it an excellent dopant for contributing empty d bands to reduce both the band gap and the optical gap. In this way, after Ni^{3+} formation and resonant energy transfers through the layered structure, PIRET initiates OER and enhanced kinetics.

Moreover, LDHs are known as materials with relatively good structural stability. However, their long-term performance under continuous irradiation and in aqueous environments may be affected by phase transformation or leaching of metal ions. Similarly, plasmonic nanoparticles can undergo morphological changes or surface oxidation over time, which leads to the reduction of their photocatalytic enhancement effects. Future work will be necessary to optimize the composite structure and surface passivation to enhance long-term stability for practical applications. Our experimental observations support our viewpoint that the changes in the electronic structure that drive enhanced photocatalytic activity of the doped LDH materials are not due to structural changes, but are a consequence of the introduction of in-gap states by the dopants. The identity of the dopant(s) thus plays a crucial role in regulating the contribution of the PIRET process. Notably, dopants have been shown experimentally[11] to impact the potential of the Ni^{2+}/Ni^{3+} redox couple, with a negative (positive) shift associated with Co (Fe) dopants,[3] even though the onset potential and more importantly, the thermoneutral potential are affected minimally. It is clear that the onset of the OER potential in the LDH structures is driven by electronic mechanisms involving changes in electronic structures and effects of dopants.

Furthermore, the present results can be rationalized in terms of the Resonant Energy Transfer model of King *et al.*[56] while this formalism has been applied to a real case in ref. 57. As discussed above, since AuNPs and NiFeLDH possess an energy gap of nearly the same size, they can be coupled resonantly to drive the PIRET mechanism, whose efficiency and spatial range can be estimated using the near-field resonance of electric dipoles along the lines of ref. 1. Fig. S19(a) depicts the efficiency of the energy transfer process as a function of distance R, while Fig. S19(b) shows that for R = 2 nm, exciton transfer from AuNPs occurs within a few femtoseconds. Interestingly, the exciton transfer exhibits a damped oscillatory behavior depending on the exciton lifetime, indicating that exciton transport can resemble coherent behavior rather than the usual diffusion-like transport.

4. Conclusion

In summary, we successfully synthesized and characterized the structure of α-$Ni(OH)_2$ LDH and its doped structures *i.e.*, NiFeLDH, and NiFeCoLDH. We confirmed experimentally and theoretically, that modifying the pristine $Ni(OH)_2$ LDH has a great impact on its electronic and optical properties. More specifically, the introduction of single Fe atom and co-doped Fe and Co atoms into the lattice structure of α-$Ni(OH)_2$ reduces its large band gap and introduces additional flat bands. Also, we studied the effect of coupling these LDH materials with AuNPs on catalyzing the OER, thereby proposing the non-radiative energy transfer mechanism between the AuNP and the LDH materials through electromagnetic field-mediated dipole–dipole interaction, namely PIRET. The produced in-gap states introduced by the dopants, specifically Fe, provide resonance channels with the AuNP surface plasmon peak at about 2.5 eV, facilitating the occurrence of the PIRET mechanism. The highly efficient PIRET mechanism indicates a great role in boosting the photocatalytic activity of the LDH catalysts for OER. Our results offer insights into developing photocatalytically active catalysts using doping techniques. This work offers doping techniques as a promising approach to manipulate the band structure, thereby facilitating the occurrence of the PIRET mechanism in the resulting photocatalyst and consequently boosting the OER.

Author contributions

Conceptualization, B. W. K., P. N., B. B., D. L., S. S. D. and S. M.; methodology, B. W. K., P. N., B. B., D. L., S. S. D., and S. M.; formal analysis, B. W. K., P. N., H. C., and S. S. D.; investigation, B. W. K., P. N., H. C., S. S. D., and S. M.; resources, P. N., S. S. D., and S. M.; data curation, B. W. K., P. N., and H. C.; writing – original draft, B. W. K., P. N., and S. S. D.; writing – review and editing, B. W. K., P. N., B. B., D. L., A. B., S. S. D., and S. M.; visualization, B. W. K., P. N., and H. C.; supervision, S. S. D. and S. M.; project administration, S. S. D. and S. M.; funding acquisition, P. N., S. S. D., and S. M.

Conflicts of interest

The authors declare no competing interests.

Data availability

The data supporting this article have been included as part of the SI.

Document S1. Supplemental experimental procedures and data. Fig. S1–S19 and Tables S1–S8 including tandem electron microscopy images and UV-vis spectra of synthesized materials; cyclic voltammagrams for nickel-based LDHs; crystal cell structures constructed for modeling purposes; parameters of band structure calculations in CASTEP; X-ray diffraction spectra of Ni-based LDHs with and without gold decoration; Le Bail XRD fitting for Ni-based LDHs; phase quantitation results for α-$Ni(OH)_2$; Kubelka–Munk transformations and band gap estimation of Ni-based LDHs; differences in atomic position between optimized and unoptimized crystal cell structures; energies, Bader charges and band structures of crystal cells; projected density of states of Ni-based LDHs; calculated dielectric functions of Ni-based LDHs; calculated refractive index of Ni-based LDHs. Data file S1. NiLDH_structures.zip. Cartesian

coordinates of structures used in simulations. See DOI: https://doi.org/10.1039/d5cp01022e

Acknowledgements

The authors sincerely appreciate the funding support from the Army Research Office (Grant no. W911NF-19-1-0164) and encouragement from Dr Robert Mantz without which this would not have happened. P. N. gratefully acknowledges the support of the Fund of Scientific Research Flanders (FWO), Belgium, Grant number 1261721N. P. N. and D. L. acknowledge the computational resources and services provided by the VSC (Flemish Supercomputer Center) and the HPC infrastructure of the University of Antwerp (CalcUA), both funded by the FWO - Vlaanderen and the Flemish Government, Department EWI. B. W. K., H. C., and S. S. D gratefully acknowledge Northeastern University for providing the startup funding and the National Science Foundation for supporting this work in part through a Research Experiences for Undergraduates (REU) Site grant under award no. NSF CHE-1757078. B. W. K., H. C., and S. S. D. also acknowledge the computing resources from Northeastern University Research Computing and from the Extreme Science and Engineering Discovery Environment (XSEDE), which is supported by National Science Foundation grant number ACI-1548562. B. B. gratefully acknowledge that the work at LUT was supported by the INERCOM platform, and the CSC—IT Centre for Science, Finland, is acknowledged for providing computational support. A. B. acknowledges support of Massachusetts Technology Collaborative through award number MTC-22032 and the resources of the Quantum Materials and Sensing Institute. We thank the assistance of Ian Kendrick in synthesis and electrochemical measurements, Yongmin Liu and Chuangtang Wang in electrochemical measurements, and Don Heiman for the magnetic measurements.

References

1 S. Naseem, B. Gevers, R. Boldt, F. J. W. J. Labuschagné and A. Leuteritz, *RSC Adv.*, 2019, **9**, 3030–3040.
2 C. Xing, F. Musharavati, H. Li, E. Zalezhad, O. K. S. Hui, S. Bae and B.-Y. Cho, *RSC Adv.*, 2017, **7**, 38945–38950.
3 X. Wang, H. Zhong, S. Xi, W. S. V. Lee and J. Xue, *Adv. Mater.*, 2022, **34**, 2107956.
4 H. Bode, K. Dehmelt and J. Witte, *Electrochim. Acta*, 1966, **11**, 1079–1087.
5 A. Van der Ven, D. Morgan, Y. S. Meng and G. Ceder, *J. Electrochem. Soc.*, 2006, **153**, A210.
6 B. Zhang, X. Zheng, O. Voznyy, R. Comin, M. Bajdich, M. García-Melchor, L. Han, J. Xu, M. Liu, L. Zheng, F. P. García de Arquer, C. T. Dinh, F. Fan, M. Yuan, E. Yassitepe, N. Chen, T. Regier, P. Liu, Y. Li, P. De Luna, A. Janmohamed, H. L. Xin, H. Yang, A. Vojvodic and E. H. Sargent, *Science*, 2016, **352**, 333–337.
7 L. J. Enman, M. B. Stevens, M. H. Dahan, M. R. Nellist, M. C. Toroker and S. W. Boettcher, *Angew. Chem., Int. Ed.*, 2018, **57**, 12840–12844.
8 M. B. Stevens, L. J. Enman, E. H. Korkus, J. Zaffran, C. D. M. Trang, J. Asbury, M. G. Kast, M. C. Toroker and S. W. Boettcher, *Nano Res.*, 2019, **12**, 2288–2295.
9 F. Dionigi and P. Strasser, *Adv. Energy Mater.*, 2016, **6**, 1600621.
10 Q. Zhou, Y. Chen, G. Zhao, Y. Lin, Z. Yu, X. Xu, X. Wang, H. K. Liu, W. Sun and S. X. Dou, *ACS Catal.*, 2018, **8**, 5382–5390.
11 M. K. Bates, Q. Jia, H. Doan, W. Liang and S. Mukerjee, *ACS Catal.*, 2016, **6**, 155–161.
12 M. W. Louie and A. T. Bell, *J. Am. Chem. Soc.*, 2013, **135**, 12329–12337.
13 M. A. Oliver-Tolentino, J. Vázquez-Samperio, A. Manzo-Robledo, R. D. G. González-Huerta, J. L. Flores-Moreno, D. Ramírez-Rosales and A. Guzmán-Vargas, *J. Phys. Chem. C*, 2014, **118**, 22432–22438.
14 O. Diaz-Morales, I. Ledezma-Yanez, M. T. M. Koper and F. Calle-Vallejo, *ACS Catal.*, 2015, **5**, 5380–5387.
15 J.-C. Chen, C.-T. Hsu and C.-C. Hu, *J. Power Sources*, 2014, **253**, 205–213.
16 X. Chen, C. Long, C. Lin, T. Wei, J. Yan, L. Jiang and Z. Fan, *Electrochim. Acta*, 2014, **137**, 352–358.
17 Y. Yang, S. Wei, Y. Li, D. Guo, H. Liu and L. Liu, *Appl. Catal., B*, 2022, **314**, 121491.
18 J. H. Lee, H. J. Lee, S. Y. Lim, K. H. Chae, S. H. Park, K. Y. Chung, E. Deniz and J. W. Choi, *Adv. Funct. Mater.*, 2017, **27**, 1605225.
19 Y. Wang, J. Zhang, W. Liang, W. Qin, Y. Sun and L. Jiang, *Adv. Energy Sustainability Res.*, 2021, **2**, 2100092.
20 L. Mascaretti, A. Dutta, Š. Kment, V. M. Shalaev, A. Boltasseva, R. Zbořil and A. Naldoni, *Adv. Mater.*, 2019, **31**, 1805513.
21 Y. Shi, J. Wang, C. Wang, T.-T. Zhai, W.-J. Bao, J.-J. Xu, X.-H. Xia and H.-Y. Chen, *J. Am. Chem. Soc.*, 2015, **137**, 7365–7370.
22 Z. Yin, B. Chen, M. Bosman, X. Cao, J. Chen, B. Zheng and H. Zhang, *Small*, 2014, **10**, 3537–3543.
23 G. Liu, P. Li, G. Zhao, X. Wang, J. Kong, H. Liu, H. Zhang, K. Chang, X. Meng, T. Kako and J. Ye, *J. Am. Chem. Soc.*, 2016, **138**, 9128–9136.
24 C. Ye, M.-Q. Wang, S.-J. Bao and C. Ye, *ACS Appl. Mater. Interfaces*, 2019, **11**, 30887–30893.
25 S.-M. Xu, H. Yan and M. Wei, *J. Phys. Chem. C*, 2017, **121**, 2683–2695.
26 M. Piccinni, S. Bellani, G. Bianca and F. Bonaccorso, *Inorg. Chem.*, 2022, **61**, 4598–4608.
27 O. Aalling-Frederiksen, N. Schlegel, S. Punke, A. S. Anker, G. K. H. Wiberg, B. Wang, J. Edelvang-Pejrup, F. B. Holde, M. P. Salinas-Quezada, N. P. L. Magnard, L. G. Graversen, M. Arenz, R. K. Pittkowski and K. M. Ø. Jensen, *Small*, 2025, **21**, 2411211.
28 D. S. Hall, D. J. Lockwood, C. Bock and B. R. MacDougall, *Proc. R. Soc. A: Math. Phys. Eng. Sci.*, 2015, **471**, 20140792.

29 M. Rajamathi, P. Vishnu Kamath and R. Seshadri, *J. Mater. Chem.*, 2000, **10**, 503–506.
30 R. Attias, K. Vijaya Sankar, K. Dhaka, W. Moschkowitsch, L. Elbaz, M. Caspary Toroker and Y. Tsur, *ChemSusChem*, 2021, **14**, 1737–1746.
31 F. Dionigi, Z. Zeng, I. Sinev, T. Merzdorf, S. Deshpande, M. B. Lopez, S. Kunze, I. Zegkinoglou, H. Sarodnik, D. Fan, A. Bergmann, J. Drnec, J. F. D. Araujo, M. Gliech, D. Teschner, J. Zhu, W.-X. Li, J. Greeley, B. R. Cuenya and P. Strasser, *Nat. Commun.*, 2020, **11**, 2522.
32 A. Le Bail and A. Jouanneaux, *J. Appl. Crystallogr.*, 1997, **30**, 265–271.
33 A. Iranzo and F. M. Mulder, *Mater. Adv.*, 2021, **2**, 5076–5088.
34 C. C. L. McCrory, S. Jung, J. C. Peters and T. F. Jaramillo, *J. Am. Chem. Soc.*, 2013, **135**, 16977–16987.
35 N. Pourshirband and A. Nezamzadeh-Ejhieh, *J. Mol. Liq.*, 2021, **335**, 116543.
36 P. Kubelka, *Z. Tech. Phys.*, 1931, **12**, 596–601.
37 S. J. Clark, M. D. Segall, C. J. Pickard, P. J. Hasnip, M. I. J. Probert, K. Refson and M. C. Payne, *Z. Kristallogr. – Cryst. Mater.*, 2005, **220**, 567–570.
38 G. Kresse and J. Furthmüller, *Comput. Mater. Sci.*, 1996, **6**, 15–50.
39 R. L. Doyle, I. J. Godwin, M. P. Brandon and M. E. G. Lyons, *Phys. Chem. Chem. Phys.*, 2013, **15**, 13737–13783.
40 J. Kang, Y. Xue, J. Yang, Q. Hu, Q. Zhang, L. Gu, A. Selloni, L.-M. Liu and L. Guo, *J. Am. Chem. Soc.*, 2022, **144**, 8969–8976.
41 R. F. Bader, *Acc. Chem. Res.*, 1985, **18**, 9–15.
42 M. Gajdoš, K. Hummer, G. Kresse, J. Furthmüller and F. Bechstedt, *Phys. Rev. B: Condens. Matter Mater. Phys.*, 2006, **73**, 045112.
43 J. Hu, D. Jiang, Z. Weng, Y. Pan, Z. Li, H. Du and Y. Yuan, *Chem. Eng. J.*, 2022, **430**, 132736.
44 Z. Xu, Y. Ying, G. Zhang, K. Li, Y. Liu, N. Fu, X. Guo, F. Yu and H. Huang, *J. Mater. Chem. A*, 2020, **8**, 26130–26138.
45 J. Li and N. Wu, *Catal. Sci. Technol.*, 2015, **5**, 1360–1384.
46 R. V. D. Krol and M. Grätzel, *Photoelectrochemical hydrogen production*, Springer, New York, 2012.
47 S. K. Cushing and N. Wu, *J. Phys. Chem. Lett.*, 2016, **7**, 666–675.
48 C. Sönnichsen, T. Franzl, T. Wilk, G. von Plessen, J. Feldmann, O. Wilson and P. Mulvaney, *Phys. Rev. Lett.*, 2002, **88**, 077402.
49 S. K. Cushing, A. D. Bristow and N. Wu, *Phys. Chem. Chem. Phys.*, 2015, **17**, 30013–30022.
50 S. K. Cushing, J. Li, F. Meng, T. R. Senty, S. Suri, M. Zhi, M. Li, A. D. Bristow and N. Wu, *J. Am. Chem. Soc.*, 2012, **134**, 15033–15041.
51 J. Li, S. K. Cushing, F. Meng, T. R. Senty, A. D. Bristow and N. Wu, *Nat. Photonics*, 2015, **9**, 601–607.
52 A. Furube, L. Du, K. Hara, R. Katoh and M. Tachiya, *J. Am. Chem. Soc.*, 2007, **129**, 14852–14853.
53 C. Clavero, *Nat. Photonics*, 2014, **8**, 95–103.
54 L. Demourgues-Guerlou and C. Delmas, *J. Power Sources*, 1993, **45**, 281–289.
55 C. Liu, L. Huang, Y. Li and D. Sun, *Ionics*, 2010, **16**, 215–219.
56 C. King, B. Barbiellini, D. Moser and V. Renugopalakrishnan, *Phys. Rev. B: Condens. Matter Mater. Phys.*, 2012, **85**, 125106.
57 S. Das, C. Wu, Z. Song, Y. Hou, R. Koch, P. Somasundaran, S. Priya, B. Barbiellini and R. Venkatesan, *ACS Appl. Mater. Interfaces*, 2019, **11**, 30728–30734.

